Time Series Modelling for Dynamic Thermal Rating of Overhead Lines

Junpeng Zhan, *Member, IEEE,* C. Y. Chung, *Fellow, IEEE*, and Elemer Demeter, *Member, IEEE*

***Abstract*—Dynamic thermal rating (DTR) is more accurate and can better utilize the transmission/distribution capacity of an electric power system compared to static thermal rating. It is beneficial to integrate DTR into power system planning problems where modelling the DTR is vital. This paper presents a new modelling method for DTR that consists of three sequential steps: a multivariate polynomial regression between the DTR and its four affecting factors, an hourly normalization, and an autoregressive integrated moving average (ARIMA). Three types of polynomial regressions were developed based on the analysis of the heat balance model for calculation of the DTR. For the purpose of comparison, several other modelling methods for the DTR were designed based on a widely used wind speed modelling method. The performance of the different modelling methods was verified using case studies from Austin, USA and Wawa, Canada. The results show that the model of the DTR obtained using the proposed method is superior in terms of both probability distribution and fitting accuracy.**

***Index Terms*—Autoregressive integrated moving average (ARIMA); dynamic thermal rating (DTR); multivariate regression; time series modelling.**

I. Nomenclature

The terminology used in this paper is as follows:

D	Conductor overall diameter (m)
Gr	Grashof number (dimensionless)
I	Conductor current (A)
K_{dir}	Wind direction factor (dimensionless)
N_u	Nusselt number (dimensionless)
N_u^{for}	Nusselt number associated with forced convection (dimensionless)
N_u^{nat}	Nusselt number associated with natural convection (dimensionless)
Pr	Prandtl number (dimensionless)
Q_{s}	Intensity of global solar radiation (W/m^2)
R_e	Reynolds number (dimensionless)
R_s	Conductor roughness (dimensionless)
R_T	Electrical resistance of conductor at temperature T (Ω/m)
T_{a}	Ambient temperature (K)
T_{c}	Final equilibrium temperature of conductor (K)
T_f	Film temperature (K)
W_d	Wind direction (degree)
W_s	Wind speed (m/s)
d	Diameter of the wires in the outermost layer (m)
g	Acceleration due to gravity, 9.807 (m/s^2)
q_{c}	Convection heat loss (W/m)
q_{r}	Heat loss by radiation of the conductor (W/m)
q_{s}	Solar heat gain by the conductor surface (W/m)
y	Height above sea level (m)
α_{em}	Emissivity coefficient with respect to black body (dimensionless)
α_{s}	Solar radiation absorption coefficient (dimensionless)
γ	Density of air (kg/m^3)
δ	Angle between wind and line direction (degree)
λ_f	Thermal conductivity of the air film in contact with the conductor (W·m^{-1}·K^{-1})
μ_f	Dynamic viscosity of the air at the film temperature (kg·m^{-1}·s^{-1})
σ_{sb}	Stefan-Boltzmann constant (W·m^{-2}·K^{-4})

The work was supported in part by the Natural Sciences and Engineering Research Council of Canada (NSERC) and the Saskatchewan Power Corporation (SaskPower).

Junpeng Zhan and C. Y. Chung are with the Department of Electrical and Computer Engineering, University of Saskatchewan, Saskatoon, SK S7N 5A9, Canada (e-mail: j.p.zhan@usask.ca, c.y.chung@usask.ca).

Elemer Demeter is with the SaskPower, Regina, SK S4P 0S1, Canada (e-mail: edemeter@saskpower.com).

II. Introduction

DYNAMIC thermal rating (DTR) calculates the maximum conductor capacity based on real-time ambient and conductor conditions. Thus, the DTR is a more accurate estimation of the capacity compared to the static thermal rating that is usually estimated under conservative conditions. The DTR is often higher but can also sometimes be lower than the static thermal rating [1,2,3,4,5]. This means that the DTR can better utilize the capacity of existing electric power systems without any overestimation of the capacity under extremely adverse conditions.

Due to the extra capacity provided by the DTR, investment in new transmission/distribution capacity can be deferred or avoided and network congestion can also be mitigated [1], implying a substantial financial benefit. Consequently, the DTR has received considerable attention and has become an important smart grid technology.

A DTR system consists of sensing and communication devices and the software to determine the DTR for the conductors [1]. Due to the development of advanced sensing and communication technologies and decreasing costs thereof, DTR systems are now suitable for commercial installation [6,7]. A number of demonstration programs have been set up to investigate the impacts of the DTR on power systems, including projects conducted by the U.S. Department of Energy [1] as well as in the U.K. [8,9,10].

To fully recognize the benefits of DTR to power systems and to accelerate its application, much recent research has been conducted to determine the optimal number and location for DTR installations [11], low carbon operation [12], congestion management [13], reliability analysis [14,15], benefits to distribution network [16,17], fuzzy method for calculating DTR

[18], and network planning [19]. Integrating DTR in power system planning problems is of great benefit [3,19]. However, an appropriate model for DTR is vital for obtaining an accurate solution to a planning problem.

The DTR can be modelled using a Monte Carlo sampling method based on its probability density function (PDF) [19] or based on the PDF of its four affecting factors and its heat balance model [9]. Another modelling method is time series modelling, with the autoregressive integrated moving average (ARIMA) model being a widely used option [20]. In [15], a low-order ARIMA model was used to represent a DTR time series for reliability analysis. However, the ARIMA model in [15] is not suitable for modelling the DTR for prolonged periods of time, e.g., one or several years, which is necessary in a planning problem; this is because the DTR varies within a large range that is difficult to directly model using a low-order ARIMA model. To solve this problem, a new modelling method for the DTR using an ARIMA model is proposed in this paper.

The DTR is affected by four factors: wind speed and direction, ambient temperature, and solar radiation [21]. Seasonal and diurnal cycles affect the last two factors, but wind speed is volatile and significantly affects the DTR. Consequently, the DTR has both seasonal and diurnal cycles but the diurnal cycle may disappear in times of volatile wind speed. To cope with the volatility of the DTR, a multivariate regression between the DTR and its four affecting factors is proposed to reduce the large-range variation of the DTR before ARIMA modelling. To retain the seasonal and diurnal distribution of the DTR, an hourly normalization method [22,23] is incorporated in the proposed modelling method.

The rest of the paper is organized as follows. The heat balance model to calculate the DTR is introduced in Section III. Then, the ARIMA model and its identification method are given in Section IV. In Section V, the proposed modelling method for the DTR is detailed. Simulation results are given and analyzed in Section VI, and conclusions are drawn in Section VII.

III. Heat Balance Model for Dynamic Thermal Rating

The DTR can be calculated using the heat balance model, which has been investigated in both the IEEE standard [24] and the CIGRE standard [21]. These two standards were compared in [25], which shows that both give similar results with slight differences. In this paper, the latest version of the CIGRE standard [21] is adopted for calculation of the DTR.

The heat balance equation can be represented by the balance of Joule heating $I^2 \cdot R_T$ (in which I is the conductor current and R_T is the electrical resistance of the conductor at temperature T), solar heating q_s, convective cooling q_c, and radiative cooling q_r:

$$I^2 \cdot R_T + q_\mathrm{s} = q_\mathrm{c} + q_\mathrm{r}, \tag{1}$$

the detailed calculation of which is conducted according to [21], where

$$q_\mathrm{s} = \alpha_\mathrm{s} \cdot Q_\mathrm{s} \cdot D\,, \tag{2}$$
$$q_\mathrm{r} = \alpha_\mathrm{em} \cdot \sigma_\mathrm{sb} \cdot \pi \cdot D \cdot (T_\mathrm{c}^4 - T_\mathrm{a}^4)\,, \tag{3}$$
$$q_\mathrm{c} = \pi \cdot \lambda_f \cdot (T_c - T_a) \cdot N_u, \tag{4}$$
$$\lambda_f = 0.02368 + 7.23 \cdot 10^{-5} \cdot T_f - 2.763 \cdot 10^{-8} \cdot T_f^2, \tag{5}$$
$$T_f = (T_\mathrm{c} + T_\mathrm{a})/2, \tag{6}$$

in which α_s is the solar radiation absorption coefficient (set at 0.8), Q_s is the intensity of global solar radiation, D is the conductor overall diameter, α_em is an emissivity coefficient (set at 0.8), σ_sb is the Stefan-Boltzmann constant, T_c is the temperature of the conductor, T_a is the ambient temperature, λ_f is the thermal conductivity of the air film in contact with the conductor, and T_f is the film temperature.

There are two types of convection. One is natural convection, which occurs when the wind speed is zero. In this type, the Nusselt number N_u in (4) is calculated as N_u^nat using

$$N_u^\mathrm{nat} = a \cdot (Gr \cdot Pr)^m\,, \tag{7}$$
$$Gr = D^3 \cdot (T_\mathrm{c} - T_\mathrm{a}) \cdot g \cdot T_f^{-1} \cdot \gamma^2 \cdot \mu_f^{-2}, \tag{8}$$
$$Pr = 0.715 - 2.5 \cdot 10^{-4} \cdot T_f, \tag{9}$$
$$\gamma = \frac{1.293 - 1.525 \cdot 10^{-4} \cdot y + 6.379 \cdot 10^{-9} \cdot y^2}{1 + 0.00367 \cdot T_f}\,, \tag{10}$$
$$\mu_f = \left(17.239 + 0.04635 T_f - 2.03 \cdot 10^{-5} T_f^2\right) \cdot 10^{-6}, \tag{11}$$

where the values of parameters a and m depend on the various ranges of $Gr \cdot Pr$ (Grashof number · Prandtl number) as given in Table I, g is the gravitational constant, γ is the density of air, μ_f is the dynamic viscosity of air at the film temperature, and y is height above sea level.

The other type is forced convection, which depends on ambient temperature as well as wind speed and direction. In this type, N_u is calculated as N_u^for using (10) and (11) as well as

$$N_u^\mathrm{for} = K_\mathrm{dir} \cdot b \cdot R_e^{n_0}\,, \tag{12}$$
$$K_\mathrm{dir} = K_{\mathrm{dir},1} + K_{\mathrm{dir},2} \cdot (\sin\delta)^{K_{\mathrm{dir},3}}, \tag{13}$$
$$R_e = W_s \cdot D \cdot \gamma \cdot \mu_f^{-1}. \tag{14}$$

At low wind speeds (W_s), i.e., below 0.5 m/s, both the forced and natural convection may be significant and it is usually recommended to use the higher value [21], i.e., N_u is the maximum value of N_u^for and N_u^nat. Values of parameters b and n_0 depend on the various ranges of the Reynolds number R_e and conductor roughness R_s, as given in Table II where $R_s = d/[2(D-d)]$, in which d is the diameter of the wires in the outermost layer. The values of $K_{\mathrm{dir},1}$, $K_{\mathrm{dir},2}$, and $K_{\mathrm{dir},3}$ depend on the angle δ, as given in Table III. The conductor used for DTR calculation is 26/7 ACSR whose parameters such as diameter D and resistance R_T are set in the same way as Annex E.1 in [21]. The maximum surface temperature T_c, for normal operation of a conductor, varies from 50 to 80 °C in Europe and up to 100 °C in North America [26], but is set to be 100 °C in this paper.

The four ambient conditions—wind speed, wind direction, ambient temperature, and solar radiation—are used as data inputs for the heat balance model (1)-(14) to calculate the maximum current allowed I, which represents the DTR in this paper.

TABLE I
Values of a and m in (7).

Range of $Gr \cdot Pr$	a	m
(10^{-1}, 10^{2}]	1.02	0.148
(10^{2}, 10^{4}]	0.85	0.188
(10^{4}, 10^{7}]	0.48	0.25
(10^{7}, 10^{12}]	0.125	0.333

TABLE II
VALUES OF b AND n_0 IN (12).

Range of R_e	Range of R_s	b	n_0
(100, 2650]	(0, 1)	0.641	0.471
(2650, 50000]	(0, 0.05]	0.178	0.633
(2650, 50000]	(0.05, 1)	0.048	0.800

TABLE III
VALUES OF $K_{\mathrm{dir},1}$, $K_{\mathrm{dir},2}$, AND $K_{\mathrm{dir},3}$ IN (13).

Range of δ	$K_{\mathrm{dir},1}$	$K_{\mathrm{dir},2}$	$K_{\mathrm{dir},3}$
[24, 90]	0.42	0.58	0.9
(0, 24)	0.42	0.68	1.08

IV. ARIMA MODEL AND ITS IDENTIFICATION

A. Autoregressive Integrated Moving Average Model

An ARIMA model [20] can be expressed as

$$\phi_p(B)\nabla^d x_t = \theta_q(B)\varepsilon_t, \quad (15)$$

where

$$\phi_p(B) = 1 - \phi_1 B - \phi_2 B^2 - \cdots - \phi_p B^p, \quad (16)$$

$$\theta_q(B) = 1 - \theta_1 B - \theta_2 B^2 - \cdots - \theta_q B^q, \quad (17)$$

in which x_t represents the random variable to be modelled, ε_t is the white noise, and ϕ_i $(i = 1,2,\cdots,p)$ and θ_j $(j = 1,2,,\cdots,q)$ represent the autoregressive (AR) and moving average (MA) parameters, respectively. B represents a backward shift operator such that $Bx_t = x_{t-1}$ and $B\varepsilon_t = \varepsilon_{t-1}$. ∇ represents a backward difference operator such that $\nabla x_t = x_t - x_{t-1} = (1-B)x_t$. ∇^d represents a d-order difference such that $\nabla^d = (1-B)^d$. Model (15) can be denoted as ARIMA (p,d,q).

B. ARIMA Model Identification

To determine the values of (p,d,q), a method using the autocorrelation function (ACF) [20], the partial autocorrelation function (PACF) [20], and an F-criterion method [23] is proposed, and consists of two steps. Note that the ACF of a q-order MA process has a cutoff after lag q and the PACF of a p-order AR process has a cutoff after lag p, and these are useful tools to determine the order of an ARIMA model.

Step 1: Determine the initial values of (p,d,q) based on the ACF and the PACF of time series x_t and its 1st-order difference ∇x_t, i.e., the lag at which the ACF (PACF) cut off indicates the number of MA (AR) terms.

Step 2: Increase both p and q by 1 and check the F-criterion as follows:

$$F = \frac{(RSS(p,q) - RSS(p+1,q+1)) \times (N-r)}{2RSS(p+1,q+1)}, \quad (18)$$

where N is the total number of observations and $r = p + q + 2$. If $F > F_\tau(2, N-r)$, where $F_\tau(2, N-r)$ denotes the F-distribution with 2 and $(N-r)$ degrees of freedom at probability level τ, then the improvement in the residual sum of squares (RSS) from ARIMA (p,d,q) to ARIMA $(p+1,d,q+1)$ is significant at the $(1-\tau)\times 100\%$ significance level, and repeat Step 2. If $F \le F_\tau(2, N-r)$, then ARIMA (p,d,q) is adequate enough and the iteration stops.

When a time series is stationary, differencing introduces a unit root into the MA part of the model [27]. To avoid over-differencing, it is necessary to check the root of the MA part of the model. If there is a unit root in the MA part of the model, i.e., $\theta_q(B) = 0$ has a solution $B = 1$, the number of MA terms should be reduced by 1 and the order of differencing should also be reduced by 1. To avoid under-differencing, similarly reduce the number of AR terms by 1 and increase the order of differencing by 1 if there is a unit root in the AR part of the model.

V. DTR MODELLING

A. Seasonal and Diurnal Cycles of DTR and its Volatility

The time series of DTR and its four affecting factors in 10 days and in 5 years are shown in Figs. 1 and 2, respectively. Fig. 1a shows that the DTR does not always have a diurnal cycle, e.g., there is a diurnal cycle on days 3-5 but this is less clear on the other days. Among the four affecting factors, the diurnal cycles of temperature and solar radiation are more obvious than those of wind speed and direction. Comparing Figs. 1a and 1b, it could be known that the DTR and wind speed have obvious positive correlation, which indicates that the DTR is significantly affected by wind speed.

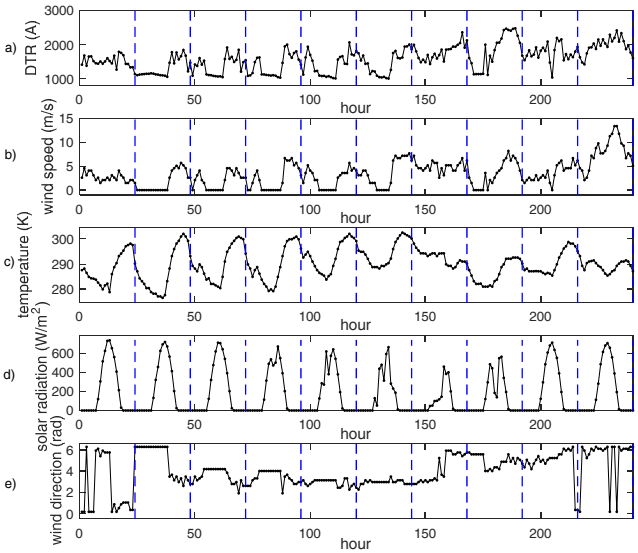

Fig. 1. Time series in 10 days where the dashed lines are used to divide different days: a) DTR, b) wind speed, c) temperature, d) solar radiation, and e) wind direction.

Figs. 2a, 2c and 2d show that the DTR, temperature, and solar radiation have seasonal cycles. Figs. 2b and 2e show that wind speed and direction do not have obvious seasonal cycles. Thus, the seasonal cycle of the DTR is caused by temperature and solar radiation.

To illustrate its volatility, DTR values for Austin, USA on the same day in years 3-5, respectively, are shown in Fig. 3a. The DTR in a given year varies significantly from hour to hour, and DTRs for the same hour but different years also span a large range. For example, the DTR increases by 1141 A from hour 3 to hour 4 in year 4 and the difference between the DTRs in the 15th hour of years 4 and 5 is 1565 A.

B. Polynomial Regression for DTR

The reason for the large variation in DTR values is the significant effect of the wind speed, which may vary greatly from hour to hour. Fig. 4 isolates the effect of each of the four factors on the DTR. The effect of wind speed is shown in the left panel; the DTR increases by 2633 A as the wind speed

increases from 0 to 20 m/s. The effects of wind direction, ambient temperature, and solar radiation on the DTR are shown in the remaining panels of Fig. 4.

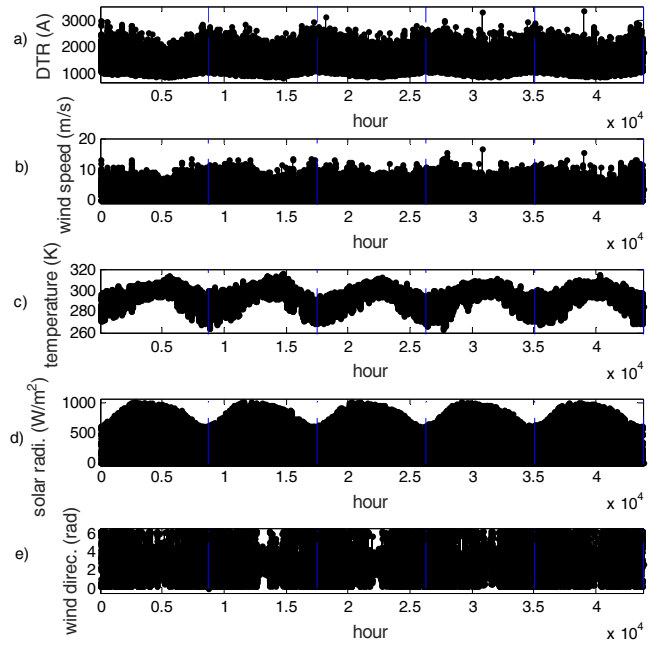

Fig. 2. Time series in 5 years where the dashed lines are used to divide different years: a) DTR, b) wind speed, c) temperature, d) solar radiation, and e) wind direction.

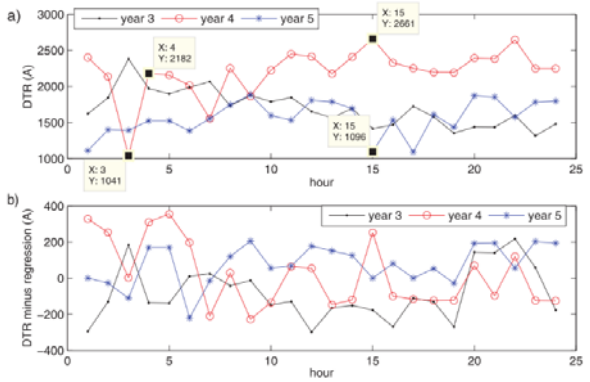

Fig. 3. Values of the DTR for Austin for the same day in three consecutive years: a) original DTR, b) DTR after subtracting the regression in (22).

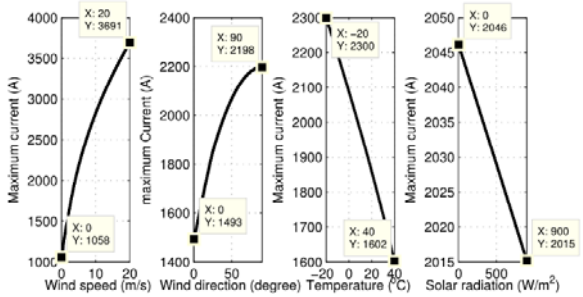

Fig. 4. DTR as a function of each of its four affecting variables: wind speed, wind direction, ambient temperature, and solar radiation.

The variation in DTR can be reduced by subtracting a regression function expressing the DTR in terms of its four affecting variables, which is the main idea of the work presented in the rest of this section. As shown in Fig. 4, the relationship between the DTR and each variable is simple and smooth. Thus, a polynomial function can be used to build a multivariate regression:

$$DTR = f_1(W_s, n_1) + f_2(W_d, n_2) + f_3(Q_s, n_3) + f_4(T_a, n_4) + c_0 + RES1, \quad (19)$$

where f_1, f_2, f_3, and f_4 are associated with the four factors, respectively; c_0 is a constant; $RES1$ represents the residual of the DTR after subtracting the regression; n_i $(i = 1,2,3,4)$ is an integer; and $f_i(x_i, n_i)$ $(i = 1,2,3,4)$ is an n_i-order polynomial function of variables x_i as given in

$$f_i(x_i, n_i) = c_{i,1} \cdot x_{i*} + c_{i,2} \cdot x_{i*}^2 + \cdots + c_{i,n_i} \cdot x_{i*}^{n_i}, \quad (20)$$

where $c_{i,j}$ $(j = 1,2,\cdots,n_i)$ is the coefficient of the polynomial function and x_{i*} is obtained by applying the following linear transformation to x_i:

$$x_{i*} = (x_i - x_i^{\min})/(x_i^{\max} - x_i^{\min}), \quad (21)$$

where $x_i^{\max}$ and $x_i^{\min}$ are the maximum and minimum values of x_i, respectively. The range of x_{i*} is 0 to 1.

Note that $x_i^{n_i}$ may be a very large number (e.g., when $x_4 = 293$ K, then $x_4^4 = 7.4 \times 10^9$), which may significantly decrease the accuracy of the regression. However, the range of $x_{i*}^{n_i}$ is 0 to 1, which prevents encountering large numbers in the regression. This is the reason to use the linear transformation (21).

As explained in Section III, the forced and natural convection are calculated via two sets of equations, respectively, that are quite different from one other. By using two different regression functions to represent the relationship between DTR and its four affecting variables under the conditions of forced and natural convection, the fitting ability of the regression should be no worse than for using just one regression function, as given in (19). This is the motivation of another regression described below.

As is usually recommended [21], the higher of the natural and forced convection values is used as the convective heat loss q_c. When the wind speed is zero, natural convection dominates. When the wind speed is higher than 0.5 m/s, forced convection dominates.

But which type of convection dominates when the wind speed is between 0 and 0.5 m/s? As recommended by [21], the angle between the wind direction and the conductor can be assumed to be 45° because there is no preferred wind direction when the wind speed is below 0.5 m/s. Then, from (7)-(14) the forced and natural convection depend only on the ambient temperature and the wind speed. To visualize the relationship between the two convection values, the difference between N_u^{for} and N_u^{nat} versus the ambient temperature and wind speed is shown in Fig. 5. The intersection of the two planes in Fig. 5 can be assumed to be a straight line represented by $W_s = -0.001756 \times (T_a - 273) + 0.2729$. Note that the units of T_a are in Kelvin (K). Thus, for wind speeds higher than $-0.001756 \times (T_a - 273) + 0.2729$, the forced convection value is higher; otherwise, the natural convection value is higher.

Now, a multivariate polynomial regression to deal with the natural and forced convection separately is

$$DTR = f_1(W_s^F, n_1) + f_2(W_d^F, n_2) + f_3(Q_s^F, n_3) + f_4(T_a^F, n_4) + f_5(W_s^N, n_5) + f_6(Q_s^N, n_6) + f_7(T_a^N, n_7) + c_0 + RES2, \quad (22)$$

where $f_i(x_i, n_i), (i = 1, \cdots, 7)$ is an n_i -order polynomial function of variables x_i as given in (20). $RES2$ is the residual of the DTR after subtracting the regression. n_i $(i = 1,2, \cdots, 7)$ is an integer. All of the n_i are set to 4 because the accuracy increases as the n_i increases from 1 to 4 but the improvement of the accuracy is small as n_i further increases. The detailed explanation of this issue is presented in Section VI-A. The superscripts *F* and *N* in (22) are associated with the forced and natural convection, respectively. f_1 , f_2 , f_3 , and f_4 are associated with the four affecting factors, respectively. Note that only three items instead of four in (22) are associated with the natural convection, i.e., f_5, f_6, and f_7; this is because wind direction does not affect natural convection.

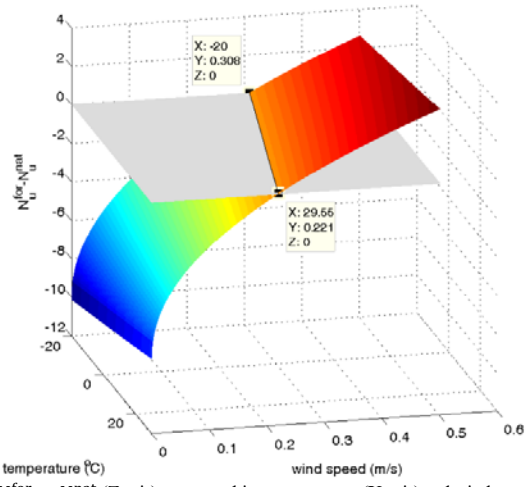

Fig. 5. $N_u^{\text{for}} - N_u^{\text{nat}}$ (Z axis) versus ambient temperature (X axis) and wind speed (Y axis), where the flat plane represents Z = 0.

There are inter-dependencies between the four different affecting factors. However, the four factors are independently considered in (22). In order to consider the inter-dependencies, a new term is added to (22) as explained in the next paragraph.

According to (3) and (4), q_s is affected by Q_s and q_r is affected by T_a, i.e., each of q_s and q_r is affected by only one factor. As mentioned above, N_u is the maximum value of N_u^{nat} and N_u^{for}. If N_u is represented by N_u^{nat}, q_c is only related to one factor, T_a, according to (7)-(11). If N_u is represented by N_u^{for}, N_u is related to three factors, T_a, W_d, and W_s, according to (11)-(14). Thus, one more term, $T_a \cdot W_d \cdot W_s$, which is associated with the forced convection is added to (22) as given in

$$DTR = f_1(W_s^F, n_1) + f_2(W_d^F, n_2) + f_3(Q_s^F, n_3) + f_4(T_a^F, n_4) + f_5(W_s^N, n_5) + f_6(Q_s^N, n_6) + f_7(T_a^N, n_7) + f_8(T_a^F \cdot W_d^F \cdot W_s^F, n_8) + c_0 + RES3, \quad (23)$$

where $f_i(x_i, n_i), (i = 1, \cdots, 8)$ is an n_i -order polynomial function of variables x_i as given in (20). $RES3$ is the residual of the DTR after subtracting the regression. n_i $(i = 1,2, \cdots, 8)$ is an integer. Similar to (22), all of the n_i are set to 4.

In (19), a data set $\{DTR, W_s, W_d, Q_s, T_a\}$ is needed to determine the coefficients of the regression. For (22), the data set could be modified to be $\{DTR, W_s, W_d, Q_s, T_a, 0,0,0\}$ or $\{DTR, 0,0,0,0, W_s, Q_s, T_a\}$ depending on whether the wind speed is higher than $-0.001756 \times (T_a - 273) + 0.2729$ or not. Then, the modified data set could be used to determine the coefficients of the regression in (22) using the same procedure as described above for (19). The procedure for determining the coefficients of the regression in (23) is the same as that for (22).

To see the effect of the regression given in (22) on reducing the variation in the DTR, the $RES2$ for Austin for the same day in years 3-5 is shown in Fig. 3b. The variation in $RES2$ is much smaller than the variation in DTR (Fig. 3a; note scale is 3-4 times as large as Fig. 3b), both considering hours in the same year and the same hour across different years. The effectiveness of (22) and the modelling procedure for the DTR are further discussed in Section VI-A.

A histogram of the DTR for Austin features two peaks (Fig. 6a). The cause for the two peaks is evident when the histogram is split into times when the forced convection is higher (Fig. 6b) or lower (Fig. 6c) than the natural convection. This allows the first and second peaks in Fig. 6a to be attributed to higher natural convection and higher forced convection, respectively.

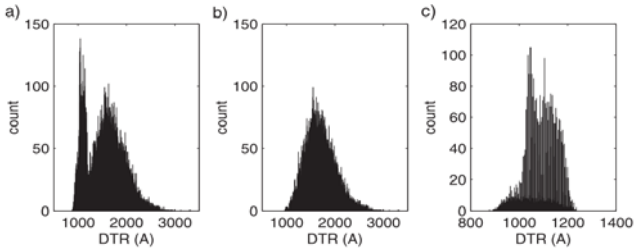

Fig. 6. Histogram of the DTR for Austin: a) All DTR values, b) DTR values for which the forced convection value is higher than natural convection value, c) DTR values for which the natural convection value is higher than forced convection value.

C. Hourly Normalization

To retain the seasonal and diurnal cycles of the DTR, an hourly normalization method used for modelling hourly wind speed [22, 23] is used. The main idea of the method is to obtain the mean and standard deviation of the original hourly data over a long period of historical time. These are then used to normalize the original hourly data using

$$x_t = (x_t^0 - \mu_t)/\sigma_t, \quad (24)$$

where x_t^0 is the original hourly data, x_t is the normalized hourly data, and μ_t and σ_t are the mean and standard deviation of the data in the *t*th hour of different years, respectively. The implementation of the hourly normalization is quite simple, i.e., calculation of μ_t and σ_t and then (24).

The $RES1$, $RES2$ and $RES3$ in (19), (22) and (23), respectively, are used as the x_t^0 in (24). The normalized data, x_t, are then used to establish an ARIMA model. This method can reproduce the high-order auto-correlation, the seasonal and diurnal distribution of the time series, over one or a few years [23].

In order to see the effect of the hourly normalization, the $RES3$ before and after the hourly normalization has been shown in Fig. 7. In Fig. 7, 9 years' data of Wawa is used and different years' data is divided by the dashed lines. It can be seen from Fig. 7 that there is seasonal cycle before the hourly normalization; that the seasonal cycle disappears after the hourly normalization; and that the range decreases from about [-500, 500] to about [-2.5, 2.5] after the hourly normalization. This makes the time series easier to be modelled by the ARIMA.

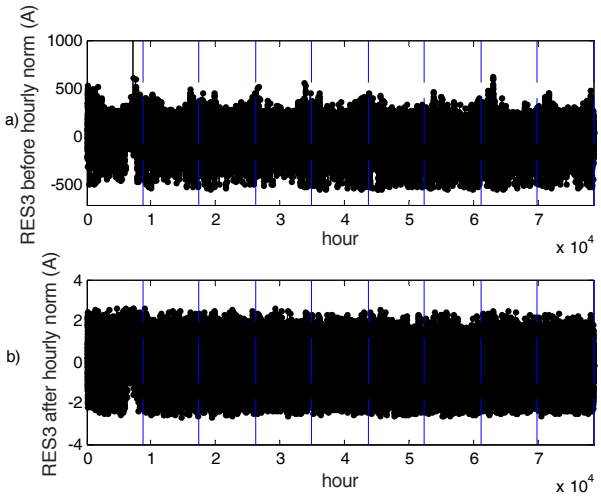

Fig. 7. The *RES*3 before and after the hourly normalization: a) before, b) after.

VI. Simulation

Wind speed, wind direction, ambient temperature, and solar radiation data for case 1 are from Austin for 1999 to 2005 and were obtained from [28]. Data for case 2 are from Wawa, Canada for 1994 to 2005 and were obtained from [29,30]. The time series modelling of the DTR is performed in R [31]. How to calculate the weather conditions around the conductors based on the weather conditions obtained from the weather stations is not the focus of this paper and it has been investigated in some other existing papers (e.g., [9]).

The DTR may have different characteristics, e.g., shape of distribution or auto-correlation, in different years. The estimated PDF of several years' worth of DTR data obtained by the 'ksdensity' function in MATLAB [32] is provided in Fig. 8, which shows the different shapes of the PDF of the DTR in different years in both cases. To cover different kinds of characteristics, several years' data are chosen to establish an ARIMA model for the DTR. For the DTR of Austin, years 3 and 6 are chosen. For the DTR of Wawa, more years are chosen to be modelled (years 4, 7, 8, and 9) as there are 12 years' worth of data to choose from.

A. Results of Different Methods for DTR Modelling

To verify the effectiveness of the proposed method for modelling the DTR, six methods are applied and compared.

- Method 1: The DTR is normalized using (24) and then modelled using (15).
- Method 2: Each of the four affecting factors of the DTR is normalized using (24) and then modelled using (15). Then, the four models are used to generate data for the heat balance model to calculate the DTR.
- Method 3: A regression for the DTR is performed using (19), then the *RES*1 in (19) is normalized using (24), and then the normalized *RES*1 is modelled using (15).
- Method 4: A regression for the DTR is performed using (23) and then the *RES*3 in (23) is modelled using (15).
- Method 5: A regression for the DTR is performed using (22), then the *RES*2 in (22) is normalized using (24), and then the normalized *RES*2 is modelled using (15).
- Method 6: A regression for the DTR is performed using (23), then the *RES*3 in (23) is normalized using (24), and then the normalized *RES*3 is modelled using (15).

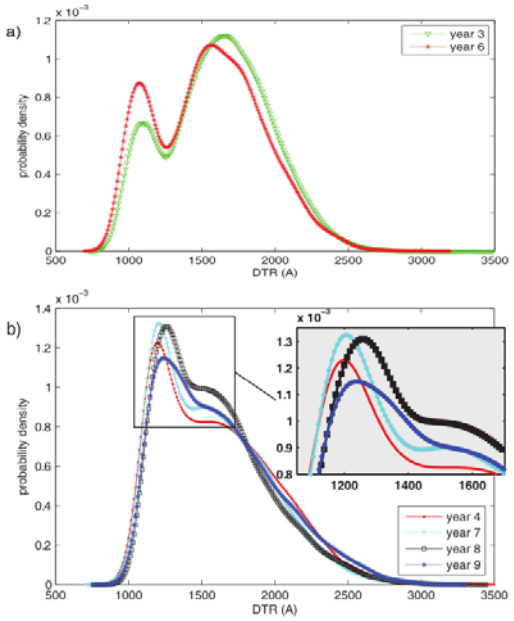

Fig. 8. The estimated probability density function of the DTR in different years for a) Austin and b) Wawa.

In Method 1, the same modelling procedure as the ARIMA modelling method for the wind speed given in [22, 23] is used to model the DTR directly. In Method 2, the same procedure as Method 1 is used to model the four affecting factors of the DTR, and the four corresponding ARIMA models obtained are used to generate the data to calculate the DTR via the heat balance model given in Section III. In the first two methods, there is no regression between the DTR and its four affecting factors. In Methods 3, 5 and 6, the three kinds of regression given in Section V-B are used, respectively. Note that the only difference between Methods 4 and 6 is whether the hourly normalization is used or not, which is used to demonstrate the effectiveness of the hourly normalization.

To compare the performance of the six methods, the estimated PDFs of the calculated DTR and the fitted DTR obtained by the six methods in the two cases are shown in Figs. 9 and 10, respectively. Note that the results shown in Figs. 9 and 10 are the PDFs of all years' data used for modelling the two cases, respectively. Figs. 9 and 10 show that the shapes of the PDFs of the DTR obtained by Methods 5 and 6 are almost the same as each other, that they are the closest to that of the calculated DTR, and that Methods 5 and 6 are a little better than Method 4 and much better than Methods 1-3 in retaining the two-peak shape of the DTR distribution.

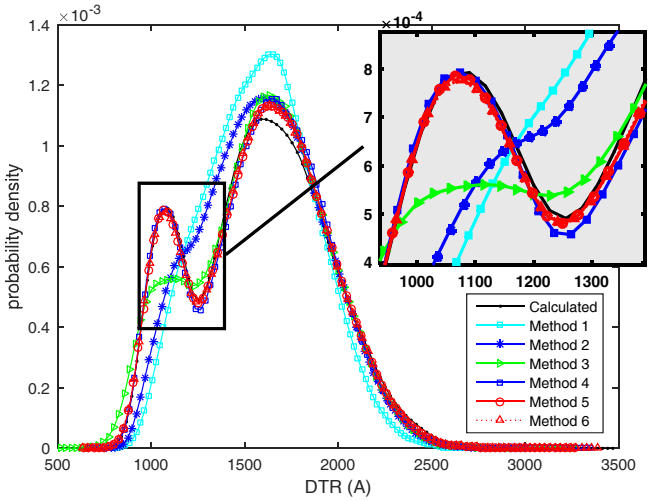

Fig. 9. The estimated probability density functions of the calculated DTR and the fitted DTR obtained by the six methods for data from Austin.

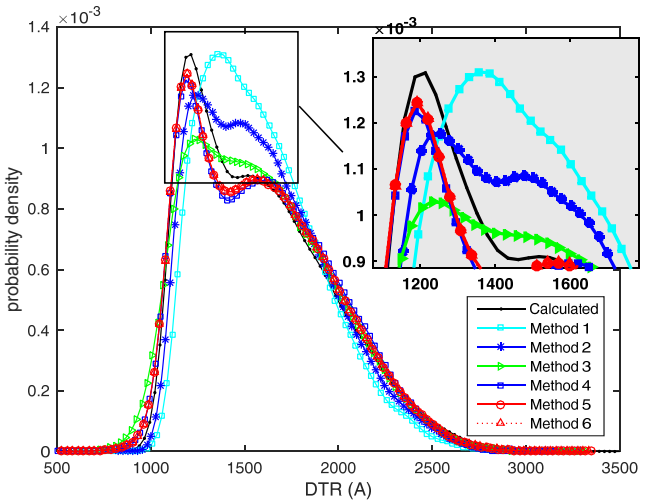

Fig. 10. The estimated probability density functions of the calculated DTR and the fitted DTR obtained by the six methods for data from Wawa.

The calculated DTR and fitted DTR obtained by the six methods in the 140th-141st days of year 3 for Austin are shown in Fig. 11, where the results of Methods 1 and 2 are provided in Fig. 11a and those of Methods 3-6 in Fig. 11b to facilitate comparison. Fig. 11 shows that Methods 5 and 6 are better than Methods 1-4 and that Methods 5 and 6 are better than Method 3 especially when the DTR is lower than 1200 A. From Fig. 6, most of the DTR below 1200 A is associated with times when natural convection dominates. Methods 5 and 6 appear to better fit the DTR compared to Method 3 when natural convection dominates. This indicates the effectiveness of (22) and (23), i.e., it is more effective to deal with the natural and forced convection separately in the multivariate polynomial regression.

To compare the modelling accuracy of the six methods, the mean absolute percentage error (MAPE) [27] between the calculated DTR and the fitted DTR obtained by each method in each case is tabulated in Table IV. Note that the smaller the MAPE, the higher the accuracy. Table IV shows that Methods 5 and 6 are more accurate than Methods 1-4 and that Method 6 is a little more accurate than Method 5, which indicates that the term that deals with the inter-dependencies of different affecting factors works but the improvement brought by this term is small. Table IV also shows that Method 6 is more accurate than Method 4, which indicates the effectiveness of the hourly normalization.

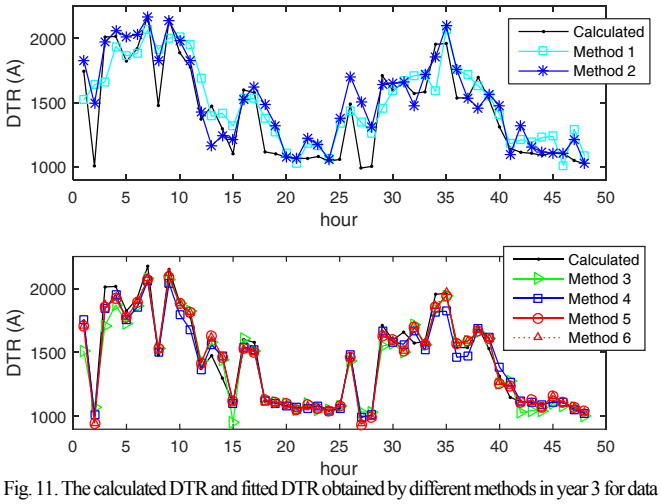

Fig. 11. The calculated DTR and fitted DTR obtained by different methods in year 3 for data from Austin: a) calculated DTR and fitted DTR obtained by Methods 1 and 2, b) calculated DTR and fitted DTR obtained by Methods 3-6.

TABLE IV
MAPE BETWEEN THE CALCULATED DTR AND THE FITTED DTR OBTAINED BY THE SIX METHODS FOR DATA FROM AUSTIN AND WAWA.

	Method 1	Method 2	Method 3	Method 4	Method 5	Method 6
Austin	10.47%	9.05%	4.20%	3.85%	3.44%	3.40%
Wawa	9.49%	8.24%	3.96%	3.47%	3.18%	3.17%

To investigate the impacts of n_i on the accuracy of the proposed method, Method 6, the MAPE between the calculated DTR and the fitted DTR obtained by Method 6 with different values of n_i for both cases is tabulated in Table V. The table indicates that the accuracy of the results increases as n_i increases from 1 to 4 but the improvement of the accuracy is small as n_i increases from 4 to 7. Thus, n_i is set to 4 in this paper.

TABLE V
MAPE BETWEEN THE CALCULATED DTR AND THE FITTED DTR OBTAINED BY METHOD 6 WITH DIFFERENT VALUES OF n_i.

n_i	1	2	3	4	5	6	7
Austin	5.56%	5.43%	4.51%	3.40%	3.39%	3.38%	3.38%
Wawa	5.24%	4.89%	3.95%	3.17%	3.12%	3.10%	3.09%

The results obtained by Method 6 for both cases are given as follows. The coefficients of the polynomial regression in (23) in both cases are given in Table VI. The ARIMA model of the normalized $RES3$ in (23) for data from Austin is $x_t - 0.7696x_{t-1} = \varepsilon_t - 0.4528\varepsilon_{t-1} - 0.0306\varepsilon_{t-2} - 0.0117\varepsilon_{t-3}$, of which more details is given in Section VI-C. The ARIMA model of the normalized $RES3$ in (23) for data from Wawa is $x_t - 0.7963x_{t-1} = \varepsilon_t - 0.4584\varepsilon_{t-1} - 0.0393\varepsilon_{t-2}$.

TABLE VI
COEFFICIENTS OF THE POLYNOMIAL REGRESSION IN (23) OBTAINED BY METHOD 6 FOR DATA FROM AUSTIN AND WAWA, RESPECTIVELY.

	$c_{1,4}$	$c_{1,3}$	$c_{1,2}$	$c_{1,1}$	$c_{2,4}$	$c_{2,3}$
Austin	-743.6	4.7×10^3	-6.9×10^3	5.3×10^3	-3.4×10^4	7.0×10^4
Wawa	7.6×10^3	-8.3×10^3	-387.0	4.1×10^3	-2.8×10^4	5.5×10^4
	$c_{2,2}$	$c_{2,1}$	$c_{3,4}$	$c_{3,3}$	$c_{3,2}$	$c_{3,1}$
Austin	-4.7×10^4	1.1×10^4	-8.3×10^5	3.1×10^6	-4.3×10^6	2.6×10^6
Wawa	-3.6×10^4	8.1×10^3	-2.6×10^5	9.5×10^5	-1.3×10^6	7.7×10^5
	$c_{4,4}$	$c_{4,3}$	$c_{4,2}$	$c_{4,1}$	$c_{5,4}$	$c_{5,3}$

Austin	235.4	-528.1	398.3	-192.0	7.7×10^5	0
Wawa	224.0	-268.4	92.3	-76.0	1.6×10^5	0
	$c_{5,2}$	$c_{5,1}$	$c_{6,4}$	$c_{6,3}$	$c_{6,2}$	$c_{6,1}$
Austin	0	0	2.3×10^5	-8.5×10^5	1.2×10^6	-7.1×10^5
Wawa	0	0	-1.9×10^4	6.4×10^4	-8.2×10^4	4.6×10^4
	$c_{7,4}$	$c_{7,3}$	$c_{7,2}$	$c_{7,1}$	$c_{8,4}$	$c_{8,3}$
Austin	29.0	-63.8	31.7	-117.2	-5.3×10^3	2.1×10^3
Wawa	15.8	-23.5	-7.3	-101.4	-8.1×10^4	6.4×10^4
	$c_{8,2}$	$c_{8,1}$	c_0			
Austin	3.0×10^3	-2.1×10^3	-6.1×10^5			
Wawa	-1.8×10^4	2.0×10^3	-1.7×10^5			

The time consumed by each kind of polynomial regression and the hourly normalization is less than 0.1 seconds and the time consumed by the ARIMA modelling is less than 10 seconds.

B. Remarks on the Applicability of the Proposed Method

The proposed method consists of three sequential steps, i.e., polynomial regression, hourly normalization, and ARIMA modelling. In the first step, the polynomial regression is designed based on the analysis of the characteristics of the CIGRE heat balance model, which is to reduce the large variation of DTR. In other words, the polynomial regression is designed based on the CIGRE model instead of some specific cases. Thus, the first step of the proposed method should be applicable to different weather conditions.

The second step is the hourly normalization, which is a widely used method [22] to reproduce the high-order auto-correlation, the seasonal and diurnal distribution of a time series, over one or a few years [23]. The third steps is the well-known ARIMA modelling which has been applied to many areas for a long time. Thus, from the viewpoint of design, the proposed method should be applicable to different weather conditions.

To verify the applicability of the proposed method, two cases (from weather stations in Wawa and in Austin and their latitudes are 48.0° N and 30.3° N, respectively) whose weather conditions are quite different from each other have been chosen for simulation analysis. The simulation results show that the proposed method has good modelling performances in these two quite-different cases. Thus, we can conclude that the proposed method should be applicable to different weather conditions.

Considering that the proposed method is applicable to these two quite-different cases, we can infer that the proposed method should be applicable if the real data measured around the conductor is used to replace the data obtained from the nearby weather station in each case. The reason is that the difference between the weather conditions around the conductor and in the nearby weather station should be much smaller than the difference between the weather conditions of the two cases. This is because the conductor and the nearby weather station are quite near to each other compared to the distance between the two weather stations in the two cases.

C. ARIMA Model Identification

As an illustration, the whole procedure to establish an ARIMA model for the $RES3$ in (23) of the DTR for data from Austin is provided in this section. First, let x_t be the normalized $RES3$ and plot the ACF and the PACF of x_t and its 1st-order difference ∇x_t, respectively, as given in Fig. 12. Note that each ACF plot in this paper starts from lag 1 instead of lag 0. Fig. 12a shows that x_t is not a stationary series and consequently a differencing is necessary. Figs. 12c and d show that a 1st-order difference is sufficient to eliminate the nonstationary aspect and that the ACF cuts off at the 3rd lag and the PACF tails off. Thus, ARIMA (0,1,3) could be assumed for x_t.

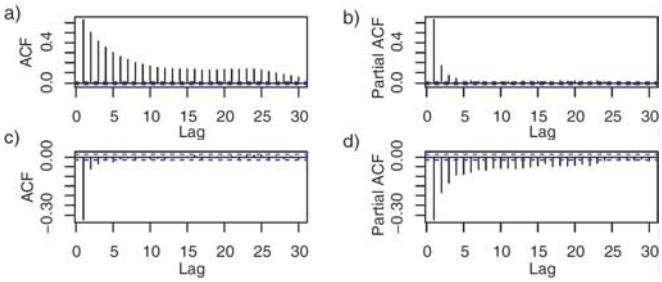

Fig. 12. The ACF and PACF of x_t and ∇x_t: a) ACF of x_t, b) PACF of x_t, c) ACF of ∇x_t, d) PACF of ∇x_t.

In the second step, both p and q increase by 1 and the model becomes ARIMA (1,1,4). The coefficients of ARIMA (1,1,4) can be obtained using the R software [31]. Then check the over-differencing of ARIMA (1,1,4), i.e., solve the equation $\theta_q(B) = 1 - 1.4192B + 0.4036B^2 + 0.0124B^3 + 0.0048B^4 = 0$. This equation has a solution $B = 1$, which indicates the existence of over-differencing. Thus, both d and q are reduced by 1 and the model becomes ARIMA (1,0,3). The values of (p, d, q), RSS, the Akaike information criterion (AIC) [27], F, and F_τ in each iteration are tabulated in Table VII, where τ is set to be 0.95, i.e., the significant level is 0.05. The AIC is used to compare the performance of different models; the smaller the AIC, the better the model fits [27]. As shown in Table VII, the improvement from iter 1 to iter 3 (the result in iter 2 is not used for F-criterion check as it is over-differencing) is significant as $F > F_\tau$, while the improvement from iter 3 to iter 4 is not significant. The values of the AIC also indicate that the model in iter 3 is the best, excluding the over-differencing model in iter 2. Thus, the model in iter 3 is adopted. That is, the best model for the normalized $RES3$ in (23) of the DTR of Austin is ARIMA (1,0,3), which could be expanded to $x_t - 0.7696x_{t-1} = \varepsilon_t - 0.4528\varepsilon_{t-1} - 0.0306\varepsilon_{t-2} - 0.0117\varepsilon_{t-3}$.

TABLE VII
ITERATIVE RESULTS FOR ARIMA MODEL IDENTIFICATION.

iter	(p, d, q)	RSS	AIC	F	F_τ
1	(0,1,3)	14834.18	46730.30	–	–
2	(1,1,4)	14521.10	46363.32	–	–
3	(1,0,3)	14525.69	46366.87	185.5	3.0
4	(2,0,4)	14525.40	46370.51	0.18	3.0

To check whether there is autocorrelation in the residual of the obtained ARIMA model, the ACF of the residual of ARIMA (1,0,3) is shown in Fig. 13 where the dashed lines indicate bounds for statistical significance. Fig. 13 shows that the autocorrelations at most lags are within the significance lines. Furthermore, the residual can pass the Box-Ljung test [27], which is used for checking the autocorrelation in residuals. Thus, there is no autocorrelation in the residual. The histogram of the residual is shown in Fig. 14, where the dashed curve is the PDF of a standard normal distribution, which indicates that the residual is very close to a normal distribution. Thus, the

residual is very close to Gaussian white noise, which justifies the suitability of the obtained ARIMA model as well as the rationality of the model identification method given in Section IV-C.

Now we can come to the conclusion that a proper model, in terms of both the probability distribution and the fitting accuracy, can be obtained by Method 6, which justifies the rationality of the whole procedure of the proposed modelling method.

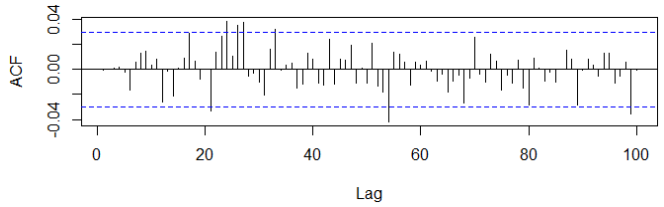

Fig. 13. ACF of the residual of the ARIMA model for the DTR for data from Austin.

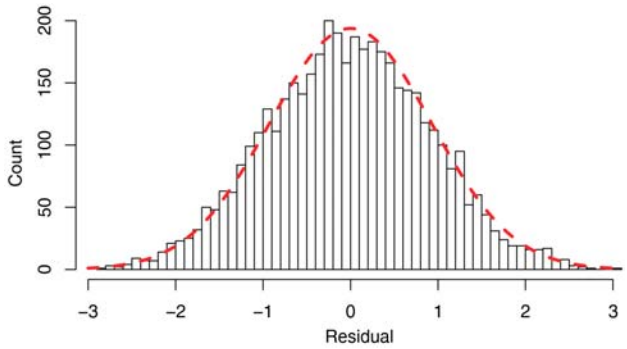

Fig. 14. Histogram of the residual of the ARIMA model for the DTR for data from Austin, where the dashed line is the PDF of a standard normal distribution.

VII. Conclusion

This paper proposes a new time-series modelling method for the DTR. The DTR is characterized by a seasonal cycle, diurnal cycle, and volatility that is caused by its four affecting factors (wind speed and direction, ambient temperature, and solar radiation). First, a multivariate regression between the DTR and its four affecting factors is proposed to reduce the large variation in the DTR. Then, an hourly normalization is used to retain the seasonal and diurnal distribution. The normalized time series is then modelled using an ARIMA model.

The performance of the proposed modelling method was verified using data from Austin and Wawa. The results show that the proposed method can result in a better model for the DTR in terms of both probability distribution and fitting accuracy compared to five other methods considered. This supports the rationality of the whole modelling procedure including the multivariate regression, the hourly normalization, and the ARIMA model identification. The proposed DTR model could be used in power system planning problems and also in the reliability analysis.

References

[1] U.S. Department of Energy, *Dynamic Line Rating Systems for Transmission Lines–Smart Grid Demonstration Program,* Topical Report, 2014.

[2] A. Phillips, B. Clairmont, D. Childs, D. Reuger, D. Douglass, J. Bell, D. Birrell, Evaluation of Instrumentation and Dynamic Thermal Ratings for Overhead Lines, Final Report, 2013.

[3] Oncor Electric Delivery Company, *Dynamic line rating*--Oncor Electric Delivery Smart Grid Program, Final Report, 2013.

[4] A. Michiorri, P. C. Taylor, S. C. E. Jupe, C. J. Berry, "Investigation into the influence of environmental conditions on power system ratings," Proc. IMechE Part A: J. Power and Energy, vol. 223, no. 7, pp. 743-757, 2009.

[5] K. W. Cheung, H. X. Wu, Implementation of Dynamic Thermal Ratings in the Operational Environment, FERC Technical Conference, June 23-25, 2014.

[6] D. Douglass, W. Chisholm, G. Davidson, I. Grant, K. Lindsey, M. Lancaster, D. Lawry, T. McCarthy, C. Nascimento, M. Pasha, J. Reding, T. Seppa, J. Toth, and P. Waltz, "Real-time overhead transmission line monitoring for dynamic rating," *IEEE Trans. Power Del.*, In Press.

[7] G. Migliavacca, *Advanced technologies for future transmission grids*. London: Springer-Verlag, 2013.

[8] S. Jupe, M. Bartlett, and K. Jackson, "Dynamic thermal ratings: The state of the art," in *CIGRE 21st International Conference on Electricity Distribution*, Frankfurt, France, 2011, pp. 1–4.

[9] A. Michiorri, P. C. Taylor, and S. C. E. Jupe, "Overhead line real-time rating estimation algorithm: description and validation," *Proc. IMechE Part A: J. Power and Energy*, vol. 224, no. A3, pp. 293–304, 2010.

[10] D. M. Greenwood, J. P. Gentle, K. S. Myers, P. J. Davison, I. J. West, J. W. Bush, G. L. Ingram, and M. C. M. Troffaes, "A comparison of real-time thermal rating systems in the U.S. and the U.K." *IEEE Trans. Power Del.*, vol. 29, no. 4, pp. 1849–1858, 2014.

[11] M. Matus, D. Saez, M. Favley, C. Suazo-Martinez, J. Moya, G. Jimenez-Estevez, R. Palma-Behnke, G. Olguin, and P. Jorquera, "Identification of critical spans for monitoring systems in dynamic thermal rating," *IEEE Trans. Power Del.*, vol. 27, no. 2, pp. 1002–1009, April 2012.

[12] J. Yang, X. Bai, D. Strickland, L. Jenkins, and A. M. Cross, "Dynamic network rating for low carbon distribution network operation–a U.K. application," *IEEE Trans. Smart Grid*, vol. 6, no. 2, pp. 988–998, 2015.

[13] F. Qiu and J. Wang, "Distributionally robust congestion management with dynamic line ratings," *IEEE Trans. Power Syst.*, vol. 30, no. 4, pp. 2198–2199, 2015.

[14] H. Shaker, H. Zareipour, and M. Fotuhi-Firuzabad, "Reliability modeling of dynamic thermal rating," *IEEE Trans. Power Del.*, vol. 28, no. 3, pp. 1600–1609, July 2013.

[15] D. M. Greenwood and P. C. Taylor, "Investigating the impact of real-time thermal ratings on power network reliability," *IEEE Trans. Power Syst.*, vol. 29, no. 5, pp. 2460–2468, 2014.

[16] A. Safdarian, M. Z. Degefa, M. Fotuhi-Firuzabad, and M. Lehtonen, "Benefits of real-time monitoring to distribution systems: Dynamic thermal rating," *IEEE Trans. Smart Grid*, vol. 6, no. 4, pp. 2023–2031, 2015.

[17] M. Z. Degefa, M. Humayun, A. Safdarian, M. Koivisto, R. J. Millar, and M. Lehtonen, "Unlocking distribution network capacity through real-time thermal rating for high penetration of DGs," *Electr. Power Syst. Res.*, vol. 117, pp. 36 – 46, 2014.

[18] H. Shaker, M. Fotuhi-Firuzabad, F. Aminifar, "Fuzzy dynamic thermal rating of transmission lines," *IEEE Trans. Power Del.*, vol. 27, no. 4, pp. 1885-1892, 2012.

[19] D. M. Greenwood and M. T. Philip, "Unlocking the benefits of real-time thermal ratings through probabilistic power network planning," *IET Gener. Transm. Distr.*, vol. 8, no. 12, pp. 2055–2064, 2014.

[20] G. E. P. Box, G. M. Jenkins, and G. C. Reinsel, *Time Series Analysis: Forecasting and Control*. Hoboken, NJ, USA: Wiley, May 2013.

[21] CIGRE Working Group B2.43, *Guide for thermal rating calculations of overhead lines*, Technical Brochure 601, Paris, France, 2014.

[22] R. Billinton, R. Karki, Y. Gao, D. Huang, P. Hu, and W. Wangdee, "Adequacy assessment considerations in wind integrated power systems," *IEEE Trans. Power Syst.*, vol. 27, no. 4, pp. 2297–2305, Nov 2012.

[23] R. Billinton, H. Chen, and R. Ghajar, "Time-series models for reliability evaluation of power systems including wind energy," *Microelectronics Reliability*, vol. 36, no. 9, pp. 1253–1261, 1996.

[24] IEEE Standard 738, *IEEE Standard for Calculation the Current-Temperature Relationship of Bare Overhead Conductors*, IEEE Standard Association: Washington, U.S.A., 2013.

[25] A. Arroyo, P. Castro, R. Martinez, M. Manana, A. Madrazo, R. Lecuna, and A. Gonzalez, "Comparison between IEEE and CIGRE thermal behaviour standards and measured temperature on a 132-kV overhead power line," *Energies*, vol. 8, no. 12, pp. 13 660–13 671, 2015.

[26] V. T. Morgan, "The thermal rating of overhead-line conductors part I. The steady-state thermal model," *Electric Power Systems Research*, vol. 5, pp. 119–139, 1982.

[27] A. K. Tangirala, *Principles of System Identification: Theory and Practice*. Boca Raton, FL, USA: CRC Press, 2015.

[28] National Oceanic and Atmospheric Administration (NOAA). [Online]. Available: ftp://ftp.ncdc.noaa.gov/pub/data/
[29] Government of Canada, *Historical Climate Data*. [Online]. Available: http://climate.weather.gc.ca/index_e.html#access
[30] ——, *Canadian Weather Energy and Engineering Datasets (CWEEDS)*. [Online]. Available: http://climate.weather.gc.ca/prods_servs/engineering_e.html
[31] R Core Team, *R: A Language and Environment for Statistical Computing*, R Foundation for Statistical Computing, Vienna, Austria, 2015. [Online]. Available: http://www.R-project.org/
[32] MATLAB and Statistics Toolbox Release 2013a. The MathWorks, Inc., Natick, Massachusetts, United States.

Junpeng Zhan (M'16) received B.Eng. and Ph.D. degrees in electrical engineering from Zhejiang University, Hangzhou, China in 2009 and 2014, respectively.

He is currently a Postdoctoral Fellow in the Department of Electrical and Computer Engineering, University of Saskatchewan, Saskatoon, SK, Canada. His current research interests include the integration of the dynamic thermal rating and renewable electric energy sources in power systems.

C. Y. Chung (M'01-SM'07-F'16) received B.Eng. (with First Class Honors) and Ph.D. degrees in electrical engineering from The Hong Kong Polytechnic University, Hong Kong, China, in 1995 and 1999, respectively.

He has worked for Powertech Labs, Inc., Surrey, BC, Canada; the University of Alberta, Edmonton, AB, Canada; and The Hong Kong Polytechnic University, China. He is currently a Professor, the NSERC/SaskPower (Senior) Industrial Research Chair in Smart Grid Technologies, and the SaskPower Chair in Power Systems Engineering in the Department of Electrical and Computer Engineering at the University of Saskatchewan, Saskatoon, SK, Canada. His research interests include smart grid technologies, renewable energy, power system stability/control, planning and operation, computational intelligence applications, and power markets.

Dr. Chung is an Editor of *IEEE Transactions on Sustainable Energy* and an Associate Editor of *IET Generation, Transmission, and Distribution*. He is also an IEEE PES Distinguished Lecturer and a Member-at-Large (Global Outreach) of the IEEE PES Governing Board.

Elemer Demeter (M'99) received his Dipl.Ing. degree in electrical engineering from the Politehnica University of Bucharest, Bucharest, Romania in 1995, his M.Sc. and Ph.D. degrees from the University of Saskatchewan, Saskatoon, SK, Canada, in 1998, and 2005, respectively. He is with the Saskatchewan Power Corporation since 1998. He is currently Manager, Engineering Protection and Control, SaskPower, Regina, SK. He holds appointments as Adjunct Professor with the University of Saskatchewan and the University of Regina, Canada. He is a Professional Engineer registered in the Province of Saskatchewan.